THE JOURNAL OF PHYSICAL CHEMISTRY C

C: Plasmonics; Optical, Magnetic, and Hybrid Materials

The Role of Zn Substitution on the Magnetic, Hyperthermic and Relaxometric Properties of Cobalt Ferrite Nanoparticles

Martin Albino, Elvira Fantechi, Claudia Innocenti, Alberto López-Ortega, Valentina Bonanni, Giulio Campo, Francesco Pineider, Massimo Gurioli, Paolo Arosio, Tomas Orlando, Giovanni Bertoni, César de Julián Fernández, Alessandro Lascialfari, and Claudio Sangregorio

J. Phys. Chem. C, **Just Accepted Manuscript** • DOI: 10.1021/acs.jpcc.8b10998 • Publication Date (Web): 15 Feb 2019

The Role of Zn^{2+} Substitution on the Magnetic, Hyperthermic and Relaxometric Properties of Cobalt Ferrite Nanoparticles

Martin Albino,[a] Elvira Fantechi,[a,b] Claudia Innocenti,[a,c] Alberto López-Ortega,[a,d] Valentina Bonanni,[a,e,§] Giulio Campo,[a] Francesco Pineider,[a,b] Massimo Gurioli,[f] Paolo Arosio,[e] Tomas Orlando,[g,†] Giovanni Bertoni,[h] Cesar de Julián Fernández,[h] Alessandro Lascialfari,[e] Claudio Sangregorio [c,a*]*

[a] Department of Chemistry "U. Schiff", University of Florence and INSTM, 50019 Sesto Fiorentino (FI), Italy

[b] Department of Chemistry and Industrial Chemistry, University of Pisa and INSTM, 56124 Pisa, Italy

[c] C.N.R. – I.C.C.O.M. and INSTM, 50019 Sesto Fiorentino (FI), Italy

[d] Instituto de Nanociencia, Nanotecnología y Materiales Moleculares and Depto. de Física Aplicada, Universidad de Castilla-La Mancha, Campus de la Fábrica de Armas, 45071 Toledo, Spain

[e] Department of Physics, University of Milan and INSTM, 20133 Milan, Italy

[f] Department of Physics and Astronomy, University of Florence, 50019 Sesto Fiorentino (FI), Italy

[g] Department of Physics and INSTM, University of Pavia, 27100 Pavia, Italy

[h] I.M.E.M- C.N.R Parco Area delle Scienze, 43124 Parma, Italy

§ Present address: IOM-CNR, Basovizza, 34149 Trieste, Italy

† Present address: Max Planck Institute for Biophysical Chemistry, 37077 Göttingen, Germany

Abstract

Zinc substitution is often proposed as an efficient strategy to improve the performances of spinel ferrite nanoparticles, particularly related to their application as theranostic agents. In this work, a series of 8 nm spinel ferrite nanoparticles of formula $Co_xZn_yFe_{3-(x+y)}O_4$, is synthesized by thermal decomposition with the purpose of investigating the role of Zn^{2+} ions in modifying the structural and magnetic properties. Contrary to most of the literature on this subject, where the sum of Co and Zn is kept constant (x+y=1), here the amount of Co is maintained at ca. x = 0.6, corresponding to the maximum of magnetic anisotropy of the Zn-undoped system, while the amount of Zn is progressively varied along the series from y = 0.05 to y = 0.4. This approach allows enlightening the effect of the Zn introduction on the magnetic and crystal structures and, particularly, on magnetic anisotropy, which is deeply investigated by several complementary techniques. A significant increase of the saturation magnetization, M_S, upon the Zn-content up to y = 0.4 is confirmed only at low temperature, while at room temperature this effect is partially nullified by the weakening of the magnetic exchange coupling constants, due to the increasing Zn substitution. Moreover, we demonstrate that the lattice modifications following the Zn introduction are responsible of a strong decrease of the particle magnetic anisotropy. Overall, these effects limit the use of Zn-substituted ferrites in biomedical applications like MRI and magnetic fluid hyperthermia, only to very low amount of Zn, as here confirmed by relaxometric and calorimetric measurements.

1. Introduction

Among the different magnetic materials, spinel ferrites nanoparticles (NPs) are intensively studied, thanks to their remarkable physical properties combined with a greater stability against oxidation with respect to metallic NPs. Recently, the interest in spinel ferrites has grown exponentially in the biomedical field, due to the many benefits envisaged by their introduction in clinical applications, such as their use as contrast agents for magnetic resonance imaging (MRI), magnetic particle imaging (MPI) and magnetic based drug-delivery systems.[1–6] Moreover, spinel ferrites can be employed as heat mediators for magnetic fluid hyperthermia (MFH), a treatment based on the high sensitivity of cancer cells to the heat locally released by NPs interacting with an alternating magnetic field.[7–9]

Up to now, the most investigated materials for biomedical applications are iron oxide spinels, i.e.,, magnetite and maghemite, mainly thanks to their biocompatibility and low toxicity. However, the introduction of low quantity of other divalent transition metal ions ($M_xFe_{3-x}O_4$, M = Zn, Co, Mn…) can be a good strategy to obtain mixed ferrites with tuned magnetic performances without compromising the biocompatibility of the pristine material. As previously reported,[10] the increase of the magnetic anisotropy, K, by the partial substitution of Fe^{2+} with Co^{2+} in iron oxide NPs of size lower than 10-12 nm leads to a significant improvement of the hyperthermic and relaxometric capability.[11,12] This issue is relevant when the size constrain is crucial as for obtaining a long circulation time in the body or to overcome the physiological barriers.[13]

Another important magnetic parameter that can be tuned for increasing the efficiency of most applications, included hyperthermia and MRI, is the spontaneous magnetization which for a nanoparticle assembly is generally identified with the saturation magnetization, M_S. A strong

enhancement of M_S has been reported after the introduction of Zn^{2+} in magnetite[14,15] or cobalt ferrite[16,17] due to cation rearrangement in the spinel lattice. In bulk materials, indeed, a gradual increase of M_S is expected with the progressive introduction of diamagnetic Zn^{2+} ions. Since the latter tend to occupy tetrahedral (T_d) sites, the antiferromagnetic coupling between Fe^{3+} in T_d and octahedral (O_h) sites is partially removed and the sublattices more unbalanced. However, this mechanism holds up until the Zn^{2+} substitution reaches *ca*. half of the total number of divalent ions.[18] For higher percentage, M_S starts decreasing, due to the weakening of the magnetic exchange between T_d and O_h sites, which induces the destabilization of the ferrimagnetic order and the local canting of the spins in the O_h sites.

Co-Zn ferrite NPs have been proposed as efficient hyperthermia mediators and MRI contrast agents, since the combined effect of increasing K by introducing Co^{2+} and M_S by Zn^{2+} substitution is expected to produce an enhancement of the hyperthermic and relaxometric efficiencies of iron-oxide based materials. However, at the nanoscale, the increase of spin disorder due to the weakening of magnetic exchange coupling becomes particularly relevant and can nullify the benefit when temperatures as those related to clinical applications are considered (300-350 K). Notwithstanding this effect, surprisingly high values of M_S at room temperature (117 emu/g,) have been reported for 15 nm NPs of zinc ferrite ($Zn_yFe_{3-y}O_4$) for y=0.4, followed by a significant decrease for further Zn inclusion.[15,16] Zn substituted cobalt ferrite NPs ($Co_xZn_yFe_2O_4$, where x+y=1) showed a similar trend, reaching the maximum (≈ 90 emu/g) at y = 0.3 at room temperature.[19]

The aim of the present work was a systematic investigation of the magnetic, hyperthermic and relaxometric properties of $Co_xZn_yFe_{3-(x+y)}O_4$ NPs synthesized by thermal decomposition, with very similar average size (8-9 nm) in order to shed light on the effect of the progressive Zn^{2+} substitution

on cobalt ferrite properties. Contrary to most of the literature on this subject, where the total amount of Co+Zn is kept constant while varying Co- and Zn-contents simultaneously ($Co_xZn_yFe_2O4$, with x+y=1), here the Co-content was fixed to *ca*. x=0.6, corresponding to the highest value of magnetic anisotropy for non-stoichiometric cobalt ferrite,[10] and the amount of Zn was varied up to y=0.4, for which the maximum of saturation magnetization is expected in bulk material. This approach allowed us to better evaluate the peculiar role of Zn inclusion on the magnetic properties of the system, which is otherwise masked by any modification in the Co content.

NPs were prepared through thermal decomposition of metal acetylacetonates in high-boiling solvents in the presence of surfactants. This technique allows an excellent control on the composition and mean size, which has been kept constant all along the NPs series. This is a crucial issue that allowed us neglecting the strong dependence of the magnetic properties on the NP volume and focusing the comparison on the variation introduced by the different composition. The synthesized series of $Co_xZn_yFe_{3-(x+y)}O_4$ NPs was characterized by low and high resolution transmission electron microscopy (TEM and HRTEM), X-ray diffraction (XRD), inductively coupled plasma - atomic emission spectrometry (ICP-AES), X-ray absorption (XAS), X-ray magnetic circular dichroism (XMCD), magneto-optical spectroscopy and SQUID magnetometry. This detailed characterization allows us shedding new light on the effect of the Zn substitution on the magnetic properties of spinel ferrite NPs. The heating and relaxometric capability of the $Co_xZn_yFe_{3-(x+y)}O_4$ NPs were then investigated and discussed on the basis of the structural and magnetic results and their potential employment in MRI and MFH applications was assessed.

2. Experimental Section

Synthesis. All the samples were prepared under inert atmosphere using commercially available reagents. Hexane (99%), benzyl ether (99%), 1,2-hexadecanediol (HDD) (97%), oleic acid (90%), oleylamine (70%), cobalt (II) acetylacetonate (97%), zinc (II) acetylacetonate hydrate, tetramethyl ammonium hydroxide solution (25% in water), cobalt chloride hexahydrate (≥ 98%) were purchased from Aldrich Chemical Co. and iron (III) acetylacetonate (99 %) from Strem Chemicals, Inc.. Absolute ethanol was purchased from Fluka. All chemicals were used as received. In the following, samples will be labeled as CoZnFeyy where yy denotes the zinc content (i.e., y = 0.13 corresponds to yy = 13). The label of the 9 nm average size NPs includes the term "_9" at the end.

8 nm $Co_xZn_yFe_{3-(x+y)}O_4$ NPs. In a typical synthesis, $Fe(acac)_3$ (0.233 g, 0.66 mmol), $Co(acac)_2 \cdot 2\ H_2O$ (0.058 g, 0.198 mmol), $ZnCl_2$ (progressive amounts from 0 to 0.119 g, 0 to 0.873 mmol, see §1 and **Table S1** in the supporting information, SI), oleylamine (0.268 g, 1 mmol) and oleic acid (0.283 g, 1 mmol) were mixed and magnetically stirred under a flow of nitrogen in benzyl ether (50 ml) for 15 min. The resulting mixture was heated to reflux (290 °C) at 9 °C/min and kept at this temperature for 15 min under a blanket of nitrogen and vigorous stirring. The black-brown mixture was cooled at room temperature by removing the heat source. Under ambient conditions, EtOH (60 ml) was added to the mixture, causing the precipitation of a black material which was magnetically separated. The obtained product was then washed several times with ethanol, dispersed in hexane, re-precipitated with ethanol, separated with a magnet, redispersed in hexane and then centrifuged (5000 rpm, 5 min). The synthesis and purification conditions for **CoFe00** are the same, but the metal/oleic acid/oleylamine ratio (1:5:5).

9 nm $Co_xZn_yFe_{3-(x+y)}O_4$ NPs. The synthesis of these samples was carried out following the same protocol (**CoZnFe11_9**) or using $CoCl_2 \cdot 6\ H_2O$ (**CoZnFe05_9**) or $Zn(acac)_2$ hydrate (**CoZnFe26_9**) as reagents.

All the products can be readily dispersed in hexane or other apolar solvents, giving stable suspensions, giving stable suspensions without aggregates, as demonstrated by DLS measurements. The hydrodynamic radius was found to increase by 1-2 nm (see **Figure S2** in the SI).

Water suspensions for relaxometric measurements were obtained by transferring NPs from organic to aqueous solution by ligand-exchange with tetrametylammonium hydroxide (TMAOH). 5 mg of the NPs were dispersed in 10 ml of a 10% wt. TMAOH aqueous solution and sonicated for 10 min. Several washings with TMAOH solution were important to ensure removal of the oleic acid, leaving the NPs with a negative surface charge enough to stabilize the dispersion. The hydrodynamic radius was estimated to increase by 3-4 nm with respect to the inorganic core. After that, the NPs were collected with a permanent magnet and re-dispersed in deionized water (5 ml, 1 mg/ml).

Characterizations. Average diameter and size distribution of NPs were determined by low resolution TEM, using a CM12 PHILIPS microscope operating at 100 kV. Samples were prepared by drop drying a diluted suspension of NPs in hexane onto 200 mesh carbon-coated copper grids. The recorded images were analyzed with the Image Pro-Plus software. The mean diameter and the size distribution of each sample were obtained by statistical analysis over 700 – 750 particles. High-resolution TEM (HREM) images and energy dispersive X-ray spectra (EDS) were acquired

at 200 kV on a JEOL JEM-2200FS equipped with a Ω filter. The NPs were dispersed in hexane and then placed dropwise onto a carbon supported grid.

Powder XRD measurements were carried out using a Bruker D8 Advance diffractometer equipped with a CuKα radiation and operating in *θ–θ* Bragg Brentano geometry at 40 kV and 40 mA. Lattice parameters, *a*, and the mean crystallite diameters, d_{XRD}, were evaluated by TOPAS software (Bruker) using the method of fundamental parameter approach considering a cubic space group *Fd-3m*. The method is based on the Scherrer equation, $d= (0.9\lambda)/(\beta \cos \theta)$ (λ wavelength of the incident X-ray, θ diffraction angle, β the full-width at half-maximum of the diffraction peaks), and also takes into account the instrumental parameters.

ICP-AES measurements were performed in triplicate by a Varian 720-ES inductively coupled plasma atomic emission spectrometer (ICP-AES). For the analysis, about 1 mg of sample was digested by concentrated *aqua regia* (HCl suprapure and HNO_3 sub-boiled in 3:1 ratio) in the presence of H_2O_2, diluted with ultrapure water (≥18 MΩ/cm) and then analyzed using Ge as internal standard. Calibration standards were prepared by gravimetric serial dilution from monostandard at 1000 mg/L. The wavelengths used for Co, Fe, Zn and Ge were 238.204, 238.892, 206.200 and 209.426 nm, respectively. For all the samples the stoichiometry was found to be close to that of a spinel ferrite, M_3O_4.

Dynamic light scattering (DLS) measurements were carried out with a Malvern Zetasizer ZS90, Malvern Instruments Ltd.

Magnetic measurements were performed using two SQUID magnetometers (Quantum Design MPMS and Cryogenic Ltd. S600) operating in the 1.8 - 350 K temperature range with applied field up to 5 T (Quantum Design) and 6.5 T (Cryogenic). Powder samples were hosted in a Teflon tape and then pressed in a pellet to prevent preferential orientation of the nano-crystallites under the

magnetic field. The obtained values of magnetization were normalized by the weight of ferrite present in the sample and expressed in emu/g of ferrite. Zero field cooled/ field cooled (ZFC/FC) curves were obtained by measuring the temperature dependence of the magnetization applying a probe magnetic field (5 mT) after cooling the sample in the absence (ZFC) or in the presence (FC) of the field.

Magnetic circular dichroism (MCD) spectroscopic data were acquired in the UV-Vis-NIR range (1.25 eV to 4.25 eV) with a home-built setup. The magnetic field is applied parallel to the propagation direction of light with an electromagnet generating a static field of 1.3 T. The polarization of light is dynamically switched between left and right helicities at 50 kHz with a photoelastic modulator. The differential absorption signal (ΔA) between the two opposite polarizations is retrieved via phase sensitive detection with a lock-in amplifier referenced at the polarization modulation frequency. A complete MCD spectrum is taken as the difference between the spectra acquired with the magnetic field applied parallel and antiparallel to the propagation direction of light. This procedure leaves out all non-magnetic contributions to the dichroic signal. Samples for MCD measurements were prepared by mixing 100 μl of each nanocrystal toluene suspension with 100 μl of a polystyrene solution (10 mg/ml) in toluene, and casting 50 μl of the mixture on a glass slide and allowing the solvent to evaporate.

XAS and XMCD measurements were performed on dried NPs of **CoFe00**, **CoZnFe05** and **CoZnFe27**, spread onto carbon tape at the circular polarization beamline of the Elettra synchrotron (Trieste, Italy). Both XAS and XMCD spectra were recorded at the Fe and Co $L_{2,3}$ edges using total electron yield (TEY) mode at 10 K in a magnetic field of 3.5 T. The XMCD signal was normalized by the area of the XAS spectrum after correcting for the background. The orbital, μ_{orb}, and spin, μ_s, components of the mean magnetic moments for Fe and Co were determined using the

sum-rule analysis.[20] The calculations have been carried out neglecting the magnetic dipole operator[21] and setting the total number of holes per formula unit to 3 for Co^{2+} ions and 13.7 for the Fe valence band.[22,23]

Calorimetric measurements of specific absorption rate (SAR) were performed using a 6 kW power supply by Fives Celes. Measurements were carried out by applying for 300 s an alternating magnetic field of 12 kA/m amplitude and 183 kHz frequency on a suspension in toluene (1.6 - 1.9 % w/w) in the presence of 7.5 mM of oleic acid and 7.5 mM of oleylamine. The temperature of the sample was recorded using an optical fiber temperature probe (Optocon-Fotemp). Samples were surrounded by polystyrene and hosted in a glass dewar, in order to thermally isolate the sample from the surroundings. SAR values were evaluated using the equation:

$$SAR = \frac{\sum_i m_i c_{pi}}{m_{Me}} \Delta T / \Delta t$$

where ΔT is the temperature increase in the interval of time Δt, m_{Me} is the total mass of metal, mi is the mass of the *i*-species and C_{pi} its specific heat. The sum is extended to all the *i* species involved in the heat exchange. Since the measurements are carried in non-adiabatic conditions, $\Delta T/\Delta t$ values were extrapolated for $t \rightarrow 0$ by considering the initial slope of the temperature kinetic curves.

The NMR-Dispersion profiles were measured on water suspensions at 300 K for all samples (except **CoZnFe05**), with different concentrations of metal (Fe+Co), i.e., 0.430 mM (**CoFe00**), 0.334 mM (**CoZnFe13**), 0.315 mM (**CoZnFe27**), 0.244 mM (**CoZnFe40**). Longitudinal nuclear relaxation times, T_1, were measured in the range 10 kHz – 60 MHz for the ^1H Larmor frequency, corresponding to an applied magnetic field from 2.3 x 10^{-4} T to 1.4 T. To cover such a range of experimental measurements, two instruments were used: a Stelar SMARtracer, working with the fast field cycling technology and pre-polarized saturation recovery sequence, for the low field range, i.e., 10 kHz – 10 MHz, and a Stelar Spinmaster with an electromagnet for the range 10 MHz

– 60 MHz. A standard saturation recovery sequence was used in the latter case. The transverse nuclear relaxation times, T_2, were also measured for each sample at the frequency ν = 60 MHz with a Carr-Purcell-Meiboom-Gill sequence.

3. Results and discussion

Synthesis and structural characterization. The $Co_xZn_yFe_{3-(x+y)}O_4$ NPs and the reference sample **CoFe00** were synthesized by thermal decomposition of iron and cobalt acetylacetonates in benzyl ether in the presence of $ZnCl_2$, oleic acid and oleylamine. In all samples the amount of cobalt was kept constant at ca. x = 0.6, corresponding to the highest magnetic anisotropy, as observed in our previous work.[10] Instead, the Zn amount, y, was varied in the range 0 - 0.4, where the maximum increase of saturation magnetization is expected.[16]

The main chemical and structural parameters of the synthesized samples are summarized in **Table 1**. The effective stoichiometry of $Co_xZn_yFe_{3-(x+y)}O_4$ was evaluated by elemental analysis (ICP-AES) and confirmed by energy dispersive spectroscopy (EDS, **Table S2** in the SI). The amount of Fe was found, within the experimental error, almost identical to that calculated using the formula 3-(x+y). TEM images are reported in **Figure 1**, together with the NP size distributions, fitted to a log-normal function. All samples are composed of spherical NPs of *ca.* 8 nm diameter.

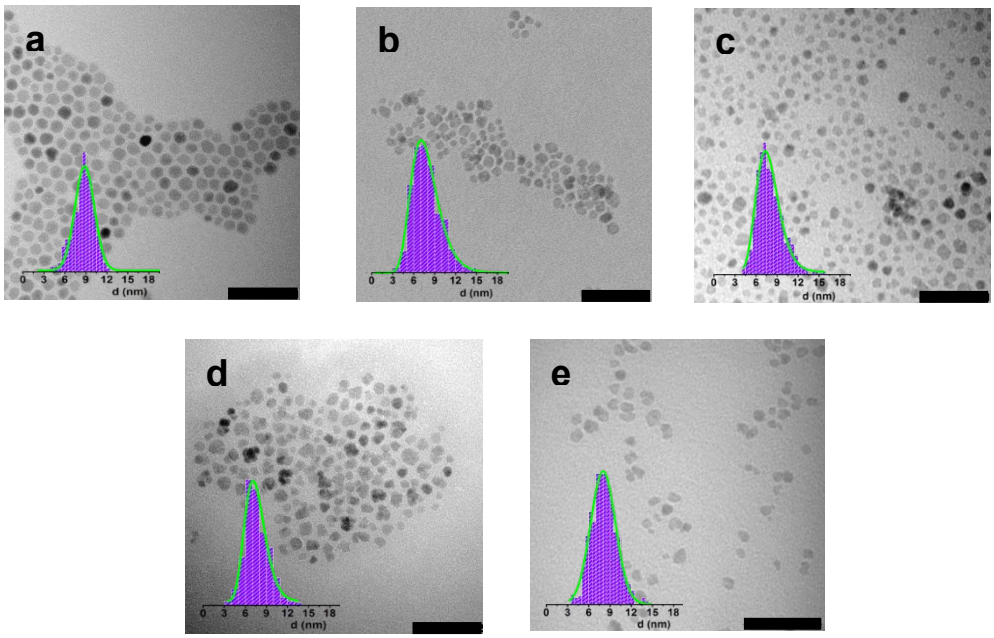

Figure 1. TEM images of $Co_xZn_yFe_{3-(x+y)}O_4$ NPs: a) **CoFe00** (d = 8.5 ± 1.9 nm), b) **CoZnFe05** (d = 7.9 ± 2.0 nm), c) **CoZnFe13** (d = 8.0 ± 1.9 nm), d) **CoZnFe27** (d = 7.6 ± 1.7 nm), e) **CoZnFe40** (d = 8.2 ± 1.8 nm). In the insets, the corresponding diameter distribution evaluated over 700-750 NPs is reported. Mean and standard deviation values are statistically evaluated from the size histograms. The continuous line represents the best-fit curve to a lognormal distribution. The scale bar corresponds to 50 nm.

Only a cubic ferrite phase is observed in the XRD patterns (**Figure 2a**): this suggests that the introduction of Zn in the reaction pool does not induce the formation of secondary phases other than the spinel. The lattice parameter increases with Zn-content (**Figure 2b** and **Table 1**) in agreement with literature data on bulk and nanostructured mixed cobalt zinc ferrites,[18,24] confirming that the Zn^{2+} ions are effectively incorporated in the ferrite lattice. Moreover, the theoretical estimation of the variation of the lattice parameter with metal ion distribution among different cavities, performed following Ref. (25) shows that a linear increase, as the one here observed, is possible only if Zn^{2+} ions replace Fe^{3+} in *Td* cavities. Finally, the good agreement between the average NP diameter obtained from TEM

and the crystal grain size from XRD measurements (**Table 1**) suggests that all samples are composed of highly ordered, single crystal NPs. The high crystallinity and the cubic spinel structure of the NPs are nicely confirmed by high resolution TEM images and electron diffraction patterns of some selected samples (**Figure S3** in SI).

Table 1. Chemical and structural properties of $Co_xZn_yFe_{3-(x+y)}O_4$ NPs.

Sample	d_{TEM} (nm)	d_{XRD} (nm)	a (Å)	x	y	z
CoFe00	8.5 ± 1.9	8.1(6)	8.387(1)	0.61	0	2.40
CoZnFe05	7.9 ± 2.0	8.5(5)	8.394(1)	0.52	0.05	2.42
CoZnFe13	8.0 ± 1.9	8.7(5)	8.399(1)	0.57	0.13	2.28
CoZnFe27	7.6 ± 1.7	6.7(6)	8.406(3)	0.59	0.27	2.11
CoZnFe40	8.2 ± 1.8	8.7(5)	8.419(1)	0.60	0.40	1.99

d_{TEM}: NP average diameter and standard deviation obtained from TEM analysis; d_{XRD}, a: crystallite mean size and lattice parameter obtained from XRD data analysis (errors on the least significant digit are reported in brackets); x, y, z: Co, Zn and Fe content obtained from ICP analysis.

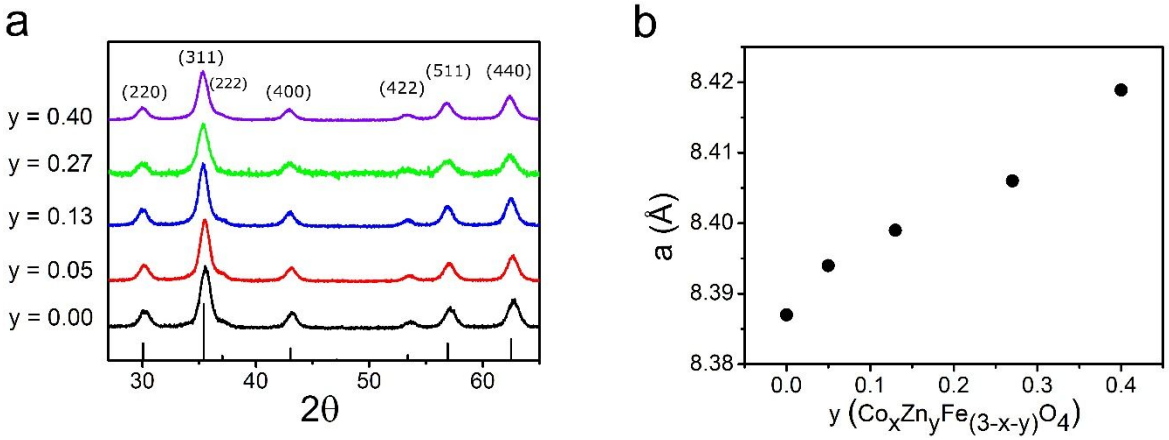

Figure 2. a) X-ray diffraction patterns of $Co_xZn_yFe_{3-(x+y)}O_4$ NPs compared to the reference pattern of cobalt ferrite (black bars); b) Lattice parameter dependence on the Zn-content, y (error is within 0.003 Å).

Magnetic and magneto-optical characterization. In **Figure 3a** the field dependence of the magnetization at low temperature (5 K) is reported. The values of coercive field, H_C, the

magnetization at 5 T, M_{5T}, and the reduced remnant magnetization, $M_R = M_{0T}/M_{5T}$, are reported in **Table 2**. At low temperature, a monotonous increase of M_{5T} with the Zn-content is observed (**Figure 3b**). This behavior can be explained by a simple model which estimates the total magnetic moment from the ion population occupying *Td* and *Oh* sites of an inverse spinel ferrite lattice (see §2 in SI). The net magnetic moment per formula unit, μ, is the sum of the individual magnetic moments of all the metal ions included in the material. The strong affinity of Zn^{2+} ions for *Td* sites[26] causes the replacement of a Fe^{3+} ion in a *Td* cavity and its migration to an *Oh* site (**Figure S4c**, SI), a hypothesis well supported by XRD and MCD data (discussed below) and by literature.[19,24,27]

Thus, considering only the spin contribution, the resulting magnetic moment per formula unit is $\mu = (4 - x + 6y)\ \mu_B$, which, for a constant Co content x = 0.6 reduces to $\mu = (3.4 + 6y)\ \mu_B$.

In **Figure 3b** the experimental M_S, approximated by M_{5T}, is compared to the theoretical one, reported as $M_S = \mu_n\ \mu_B N_A/PM$, where μ_n is the magnetic moment of ferrite in Bohr magnetons, N_A the Avogadro number and *PM* the molecular weight of $Co_xZn_yFe_{1-(x+y)}Fe_2O_4$ ferrite. A good agreement is observed only for low Zn-content ($y < 0.13$), while, for larger y, the experimental values are considerably lower. This deviation can be ascribed to the non-collinear structure of the spins inside the spinel lattice. Indeed, the progressive introduction of the diamagnetic Zn^{2+} in the *Td* sites causes a weakening of the exchange interaction between the *Oh* and *Td* sublattices, leading to a canting of the spins in the *Oh* sites with a consequent reduction of M_S.[16,28] A similar non-collinear ordering has been previously reported in $Co_{1-y}Zn_yFe_2O_4$ MNPs prepared by different experimental techniques.[16,17,26,28] It can be described with the model of Yafet-Kittel,[29] in which the *Oh* sublattice is further divided in two sub-sublattices, with magnetic moment equal in amplitude but canted in opposite directions by the same angle α_{YK} with respect to the net magnetization at 0

K. According to this model, the spin canting can be quantified by calculating α_{YK} from the experimental moment as $\mu_{exp}=m_{Oh}\cos\alpha_{YK}-m_{Td}$, where m_{Td} and m_{Oh} are the magnetic moments of the *Td* and *Oh* sublattices, respectively. The values of α_{YK} obtained are non-zero only for **CoZnFe27** (α_{YK} = 19.7°) and **CoZnFe40** (α_{YK} = 29.3°), i.e., for samples with the largest Zn-content. However, small deviations from the assumed cation distribution may also concur to the observed behavior.

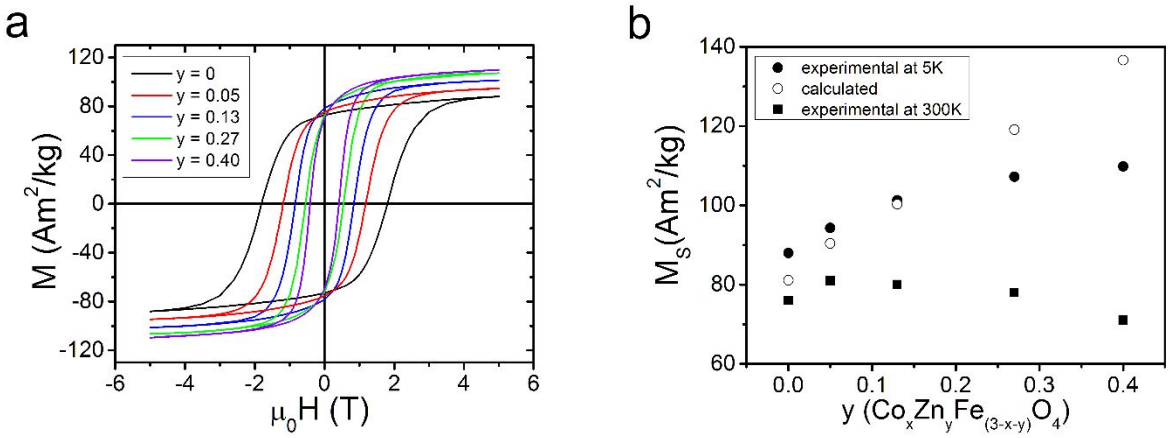

Figure 3. a) Hysteresis loops of $Co_xZn_yFe_{3-(x+y)}O_4$ NPs measured at 5 K; b) Saturation magnetization dependence on the Zn-content, *y*: experimental (full circles: 5 K; squares: 300 K) and calculated (open circles). The experimental M_S has been approximated to the high field (5 T) values.

Table 2. Magnetic and hyperthermic parameters of $Co_xZn_yFe_{3-(x+y)}O_4$.

Sample	μ_{tot}	T_B (K)	M_{5T} at 5 K (Am²/kg)	M_{5T} at 300 K (Am²/kg)	$\mu_0 H_C$ at 5 K (T)	M_R at 5 K	M_S calc. (Am²/kg)	*SAR* (W/g_{Me})
CoFe00	3.39	285	88	76	1.87	0.82	81.1	17.2 ± 2.4
CoZnFe05	3.78	~350	95	81	1.18	0.79	90.4	52.6 ± 1.3
CoZnFe13	4.21	340	101	80	0.84	0.77	100.3	46.1 ± 3.7
CoZnFe27	5.03	280	107	78	0.55	0.67	119.1	25.7 ± 4.5
CoZnFe40	5.80	250	110	71	0.42	0.63	136.6	35.5 ± 0.7

μ_{tot}: average magnetic moment in μ_B units per formula unit evaluated as $\mu = (4 - x + 6y)\ \mu_B$; T_B: blocking temperature (estimated errors less than 2%); M_{5T}: experimental magnetization measured at 5T; H_C: coercive field; M_R: reduced remnant magnetization; M_S calc. (calculated): theoretical value of saturation magnetization; *SAR*: SAR values per gram of metal (Co+Zn+Fe) obtained by applying an alternating magnetic field of 12 kA/m and 183 kHz. Errors on experimental measurement of M_{5T} and H_C can be estimated less than 1%o.

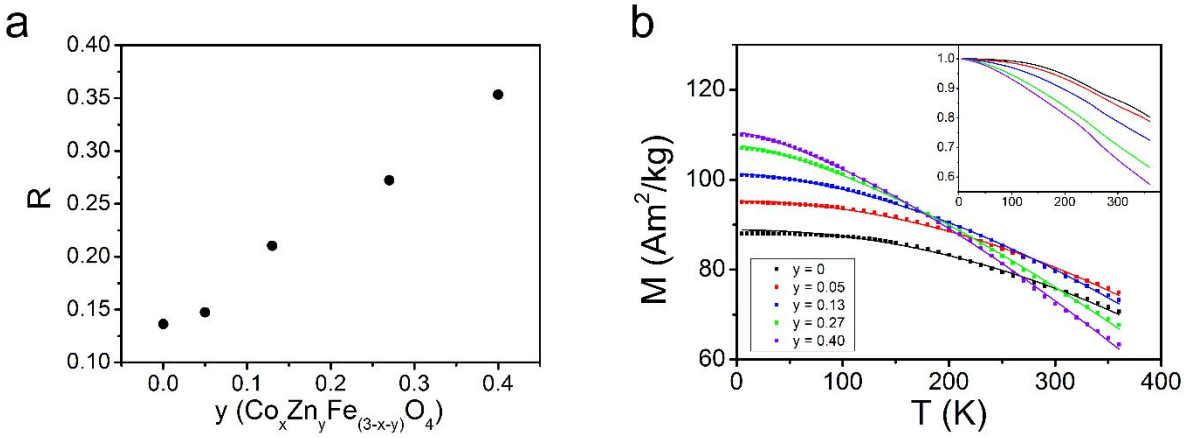

Figure 4. a) Rate of magnetization decrease with temperature, $R = [1 - M_{5T}(300K)/M_{5T}(5K)]$, of $Co_xZn_yFe_{(3-x-y)}O_4$ NPs as a function of the Zn-content *y*; b) Temperature dependence of the magnetization measured with an applied field of 5 T: continuous lines represent the best fit curves to the generalized Bloch law. In the inset, the curves are normalized to the corresponding M_{5T} measured at 5 K.

Unlike the low temperature magnetization curves, the value of M_{5T} at 300 K (**Table 2**; for the whole $M(H)$ curves see **Figure S5**, SI) does not show such a monotonous trend along the series (**Figure 3b**). The rate of magnetization decreases with temperature, expressed by the ratio $R = [1 - M_{5T}(300K)/M_{5T}(5K)]$ (**Figure 4a**), is found to increase almost linearly with the Zn-content. For a deeper analysis, the temperature dependences of M_{5T} (**Figure 4b**) were fitted to the modified Bloch law $M(T)=M_0[1-(T/T_0)^{\beta}]$, where the scaling temperature, T_0, and the exponent β are free fitting parameters. Even though strong deviations from the Bloch exponent value ($\beta = 3/2$)[30] are found especially for **CoFe00**, β shows a clear decreasing trend upon y (**Table 3**).

Deviations from the typical Bloch exponent are commonly reported for nanosized systems,[31] and are associated to cut-off of the spin wave spectra due to the reduced size of the particles, environmental conditions, like coating, interparticle interactions, or interface effects due to uncompensated layer on the particle surface. In our case, all these factors do not account for the observed trend, which can thus be attributed to the progressive weakening of the magnetic exchange coupling between ions sitting in *Td* and *Oh* cavities, induced by the Zn introduction. Additionally, T_0 is related to the exchange coupling constant, *J*, and thus it can be considered as an estimate of the Curie temperature of the material, T_c (**Table 3**).

Table 3. Generalized Bloch law best-fit parameters, T_0, β. Fitting errors are reported in brackets

Sample	β	T_0
CoFe00	2.03 (0.07)	773 (23)
CoZnFe05	1.94 (0.03)	784 (13)
CoZnFe13	1.67 (0.02)	762 (7)
CoZnFe27	1.50 (0.006)	716 (3)
CoZnFe40	1.32 (0.009)	707 (6)

As expected for nanosized materials, the estimated T_c is lower than the bulk value (826 K for $Co_{0.6}Fe_{2.4}O_4$, estimated by linear interpolation of bulk cobalt ferrite and magnetite values[32]) and it decreases with Zn-content. Similar findings are reported in the literature, where T_c were directly or indirectly estimated.[24] The different temperature dependence of M_S upon Zn-content thus accounts for the observed trend of M_{5T} at room temperature reported in **Figure 3b**, but, at the same

time, partially nullifies the magnetization increase through the introduction of Zn^{2+} ions in the cobalt ferrite lattice foreseen by temperature-independent models, as the one previously adopted.

The influence of the chemical composition on the magnetic anisotropy is investigated by analyzing the reduced remnant magnetization, M_R, and the coercive field, H_C, measured at low temperature (5 K). The decrease of M_R from 0.82 to 0.66 denotes how the cubic symmetry (typical value M_R = 0.83 - 0.87[33]) of pure cobalt ferrite evolves toward uniaxial one (typical value M_R= 0.5), without reaching it completely. Dealing with magnetic NPs of material with cubic symmetry, the evolution from a high symmetry to a lower one upon the size reduction is generally interpreted as the effect of increasing disorder of the spin alignment, particularly on the NP surface. The lattice disorder induced by the progressive introduction of Zn^{2+} ions can be therefore the responsible for the observed trend.

Assuming the reversal process occurs thorough a coherent rotation of all the spins and that interparticle interactions are weak, the effective anisotropy constant, K, is evaluated from the coercive field at 5 K (**Table 2**), as $K = H_C \cdot M_S / f$, where the saturation magnetization is again approximated by M_{5T} (5K), and the factor f is chosen f = 0.64 considering that the anisotropy is mostly cubic and positive.[34] The obtained values of K (**Figure 5**) show a marked decrease with increasing Zn concentration, particularly significant for the first substitution step for which K is reduced by 45%. Additional information can be obtained by the temperature dependence of the product $H_C \cdot M_S$, which can be associated to K only when the NPs behavior is dominated by the anisotropy energy barrier, E_a, i.e., for temperatures much lower than the blocking temperature, $T_B \propto E_a$ (**Table 2**). By definition, indeed, T_B establishes the onset of the superparamagnetic regime and it is commonly identified as the temperature at which the ZFC curve reaches its maximum, T_{max}, as for $T > T_{max}$, the magnetization behavior tends to follow the Curie law (**Figure S6** in SI).

When the reduced variable T/T_B is used, all the $H_C \cdot M_S$ data of the doped samples collapse on the same curve, whose decreasing rate for $T/T_B << 1$, thus relatable to the K decay, is faster than that of the undoped sample (inset of **Figure 5**). The different rescaling between undoped and doped samples suggests that the thermal activated reversal process is modified by the Zn introduction but does not depend on its amount.

The observed trend of K with Zn-content can be related to the structural variations induced in the ferrite lattice by the introduction of Zn^{2+} ions. One of the main contributions to the effective anisotropy is, indeed, the magneto-crystalline anisotropy, which, depending on the crystal symmetry through the spin-orbit coupling, is influenced by local crystal lattice distortions. The introduction of Zn^{2+} in the spinel structure leads to the increase of the lattice parameter, decreasing the crystal field on Co^{2+} ions in *Oh* sites, thus decreasing their magneto-crystalline anisotropy. Moreover, the introduction of Zn^{2+} ions in *Td* cavities causes a rearrangement of the distribution of Fe^{3+}, which eventually can involve Co^{2+} ions, too. This modification in the cation distribution can produce a large variation in the single ion magnetic anisotropy, which can be also responsible for the observed decrease of K.

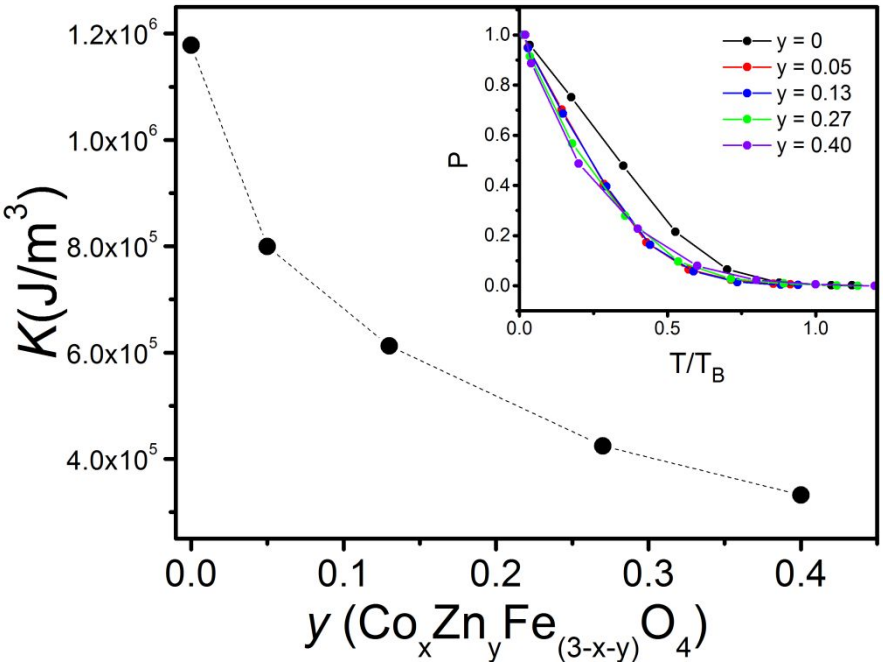

Figure 5. Anisotropy constant K of $Co_xZn_yFe_{(3-x-y)}O_4$ NPs as a function of Zn-content y. In the inset, dependence of the product $P = H_C M_S$ normalized to 5 K value on the reduced temperature T/T_B. For **CoZnFe05** T_B was extrapolated to 350 K from the H_C(T) curve, as $H_C(T \rightarrow T_B) \rightarrow 0$.

This hypothesis is supported by XMCD experiments, performed on some selected samples, which allowed the evaluation of the orbital, μ_{orb}, and spin, μ_s, components of the mean magnetic moment per ion, μ_i (**Table S3** and **Figure S7**, SI). Undoped **CoFe00** particles show the expected μ values for cobalt ferrite (4.0 μ_B and 3.4 μ_B for Fe and Co ions, respectively).[35] The incorporation of Zn^{2+} ions causes a reduction of the μ_i value at the iron edge (3.6 μ_B for y = 0.05 and 0.27) and a more marked decrease for the Co moment (2.7 μ_B for y = 0.05 and 2.4 μ_B for y = 0.27). In particular, considering the μ_{orb} and μ_s contributions separately, the inclusion of small amounts of Zn^{2+} ions causes a strong decrease of μ_{orb} of Co^{2+} ions. Since this is the main contribution to the total magneto-crystalline anisotropy of the structure, the observed reduction (*ca.* 30%), induced by the Zn substitution, can qualitatively account for the K trend.[36]

We wish to stress here that, although some works report a decrease of K with the Zn-content in Co- and Zn- co-doped ferrites,[24,37] they cannot be helpfully compared to our data, since, as already mentioned, they concern materials where the content of Co and Zn is varied simultaneously ($x+y=1$), so that the effect of increasing Zn-content on the anisotropy is masked by the changes introduced by the amount of the highly anisotropic Co^{2+} ion.

Magneto-optical spectroscopies can give important insight on the structure and composition of spinel ferrite NPs.[38,39] Room temperature MCD spectra were recorded in the UV-visible range for samples **CoZnFe13**, **CoZnFe27** and **CoZnFe40**. The representative spectrum of **CoZnFe40** is shown in **Figure 6**, along with its extinction spectrum. While the latter is mostly featureless, the MCD spectrum shows distinct peaks, owing to the additional orbital selection rule active in this type of spectroscopy.[40] Three main features dominate the spectra: a broad peak centered roughly at 3.5 eV, ascribed to intersublattice charge transfer (ISCT) transitions involving Fe ions in 2+ and 3+ oxidation states and in both *Oh* and *Td* cavities. The second feature is a peak at 2.2 eV, ascribed to intervalence charge transfer (IVCT) between Co^{2+} and Fe^{3+} in *Oh* sites. The peak at 1.7 eV is related to *d-d* transitions from Co^{2+} in *Td* cavities.[41]

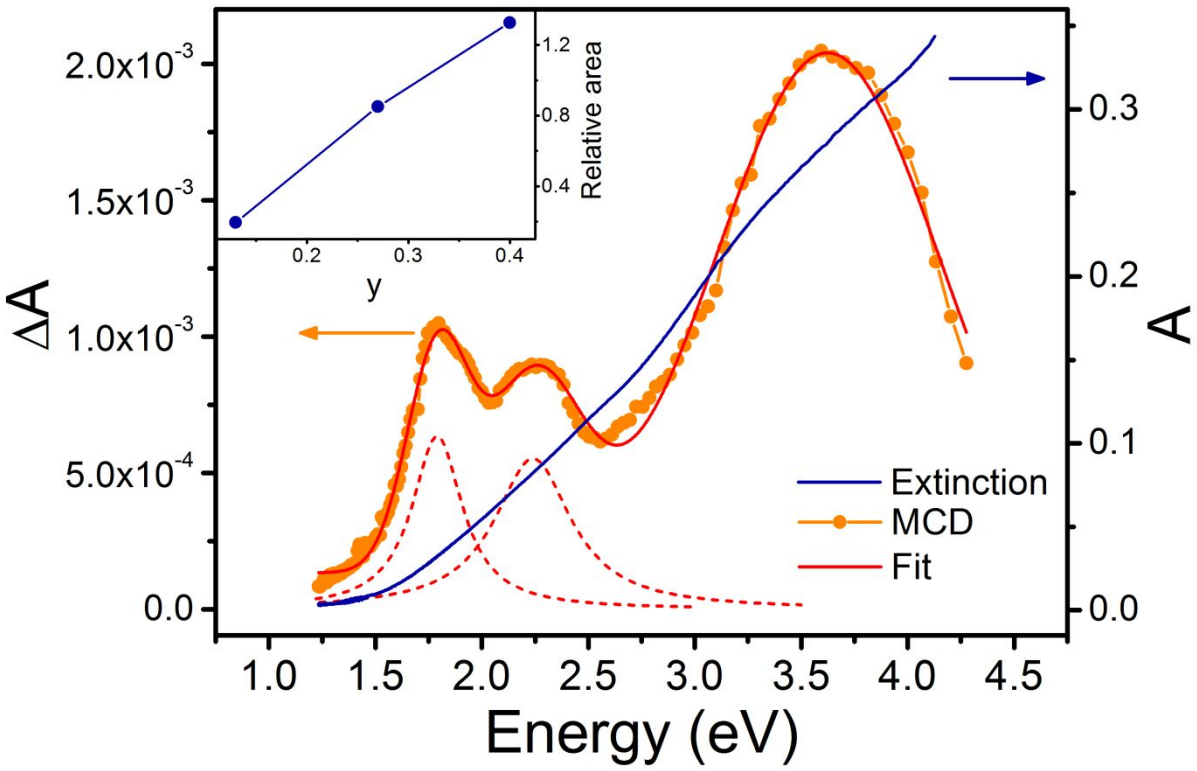

Figure 6. Extinction and MCD spectra of **CoZnFe40**. The dashed red lines represent the deconvolution of the different transitions contributing to the total spectrum (red line). Inset: ratio between the area of the peak at 1.7 eV and at 2.2 eV for samples with increasing Zn-content.

MCD spectra give us some interesting insight on cation distribution in the series. Firstly, and contrary to common schematizations, the sharp peak at 1.7 eV indicates that at least part of the population of Co^{2+} ions are situated in *Td* sites. A quantitative estimate is not straightforward, since several quantities, such as optical oscillator strength and intrinsic magneto-optical activity, are not known for the transition; however, this feature can be taken as a *caveat* that the base scheme to describe spinel and inverse spinel structures can be over-simplistic. Moreover, while no electronic transition directly involving Zn^{2+} ions is found in this photon energy interval, we can indirectly follow Zn substitution through the ratio between the peak of tetrahedral Co^{2+} *d-d* transition peak at 1.7 eV and the peak at 2.2 eV related to charge transfer transitions between octahedral Co^{2+} and

Fe^{3+} sites. According to our schematization (see §2 in the SI), Zn substitution does not influence the distribution of Co^{2+} between *Oh* and *Td* sites. Thus, the intensity of the transition at 1.7 eV involving only tetrahedral Co^{2+} is not influenced by Zn-content. On the other hand, the transition at 2.2 eV involves two types of cations: octahedral Co^{2+} ions, and octahedral Fe^{3+} species. Therefore, the occupation of *Oh* sites by Fe^{3+} cations increases as Zn is added in the structure, displacing tetrahedral Fe^{3+} ions. As a consequence, the intensity of the IVCT transition at 2.2 eV is expected to increase as Zn amount increases. If an absolute measure of the intensity of such features is not available, as in the present case, the intensity ratio between the transition at 2.2 eV and that at 1.7 eV is a good indicator of Zn^{2+} content in *Td* sites. Following this rationale, we deconvolved the two spectral contributions in all MCD spectra and evaluated their relative areas. As expected, we found a trend of the ratio described above which follows closely the effective Zn-content found from ICP (inset of **Figure 6**). This result indicates that, independently of the validity of the initial assumption, the Zn^{2+} ions occupy *Td* sites, since their position in *Oh* sites, replacing Fe^{3+} and Co^{2+}, should lead to a decrease of the transition at 2.2 eV with respect to 1.7 eV one.

Applications: hyperthermic and relaxometric efficiencies. The evaluation of the hyperthermic efficiency of the synthesized samples was performed by measuring the temperature kinetics of the $Co_xZn_yFe_{(3-x-y)}O_4$ series upon exposure to an alternating magnetic field, reported in **Figure S8** in the SI. The SAR values, estimated from the initial slope of the kinetic curves (**Table 2**), show that the introduction of Zn has an overall positive effect on the hyperthermic efficiency even though a non-monotonous increase as a function of the Zn-content is observed.

This peculiar trend of SAR can be explained only partially considering M_S, because although the M_S dependence on Zn-content is similar, its variation is very small (**Figure 7a**). On the other hand,

also K alone cannot be directly related to the SAR, as it exhibits a different trend (**Figure 5**). The magnetic behavior at field amplitudes comparable with that employed in the calorimetric measurement (H = 12 kA/m) can be useful to get information on the heating process. In **Figure 7b** the minor loops measured at room temperature are shown. Notwithstanding the minor loops are measured on a much longer time scale with respect to the hyperthermic experiments, the values of the loop area multiplied by the experimental frequency (183 kHz) can be taken as a qualitative estimation of the power losses contribution (SAR_{hl}).[42] The comparison of **Figure 7a** shows how SAR_{hl} reflects the experimental SAR trend upon Zn-content, particularly for the smallest y-value where the samples are clearly blocked (**CoZnFe05** and **CoZnFe13**). For higher Zn substitution, the minor loop area is no more a significant indicator of the heating capability of the samples, since, coherently with the T_B findings (**Table 2**), these samples are close to the superparamagnetic regime at room temperature. In this case, however, the heating mechanism is well described by the Rosenweig model, which is based on the linear response approximation, i.e $M \approx \chi H$,[43] and thus the magnetic susceptibility, χ, becomes the key parameter to assess the hyperthermic efficiency. The higher value of χ of **CoZnFe40** justifies therefore the relative raise of its SAR compared to the other samples of the series.

In the previous discussion, we evidenced how a small amount of Zn can improve the hyperthermia capability of cobalt ferrite NPs. However, the SAR value achieved is not very high, if compared to the literature data reported for ferrite NPs specifically synthesized for this application. Nevertheless, a further increase of SAR of Cobalt Zinc ferrite can be easily obtained by an even small increase of the mean size of the NPs. To support this claim, a series of NPs with 9 nm mean diameter containing the same amount of Zn and Co were synthesized. The main morphological and magnetic characterization data are reported in the SI (**Figure S9**, **Tables S4**

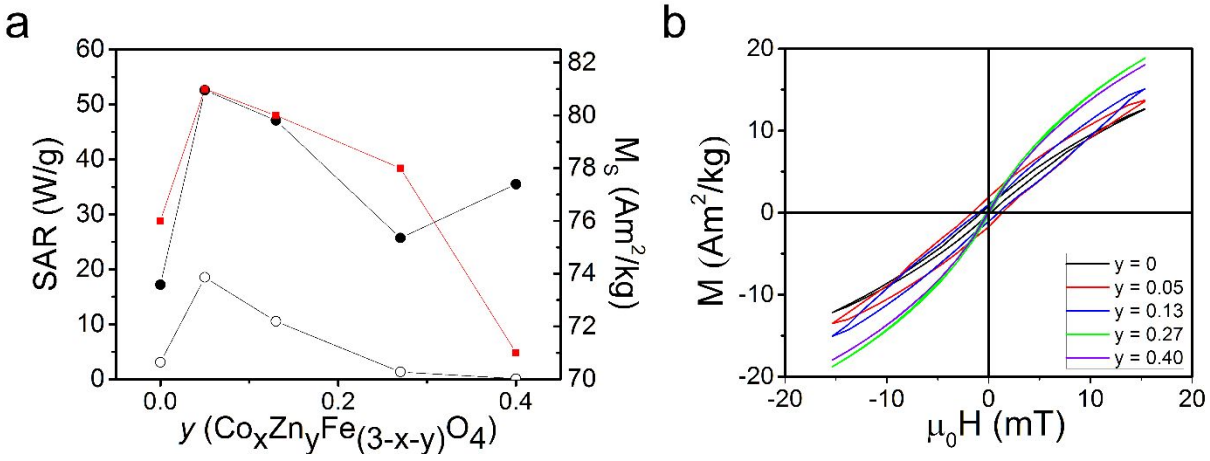

Figure7. a) *SAR* values of $Co_xZn_yFe_{(3-x-y)}O_4$ NPs as a function of Zn-content *y* experimentally measured (full circles) and evaluated by the minor loop area multiplied by the operating frequency, SAR_{hl} (empty circles); the M_S values (full squares) are reported for comparison; b) Minor loop recorded at 300K with H_{max} = 12 kA/m ($\mu_0 H_{max}$ = 15.3 mT).

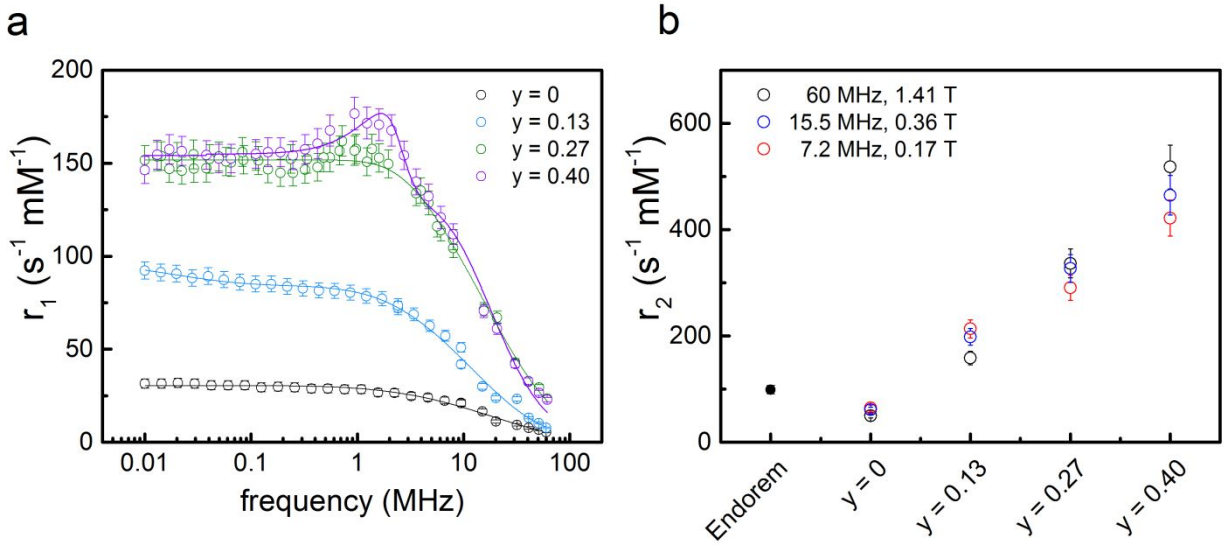

Figure 8. a) Longitudinal relaxivity profiles and best fit curves; b) Transverse relaxivities values measured at 7.2, 15.5 and 60 MHz and plotted as a function of the Zn amount. A former commercial compound (Endorem) is here used as reference (data acquired at 1.41 T).

Table 4. Best fit parameters obtained by fitting the r_1 profiles with the Roch model for nuclear relaxation**.**

Sample	τ_N(s)	r_d(nm)	M (Am^2/kg)
CoFe00	3.2 (2.4) x 10^{-7}	5.6 (0.2)	76
CoZnFe13	2.3 (0.9) x 10^{-7}	7.9 (0.3)	80
CoZnFe27	7.8 (1.1) x 10^{-8}	6.6 (0.1)	78
CoZnFe40	2.37 (1.8) x 10^{-8}	9.4 (0.3)	80

τ_N: Néel relaxation time; r_d: minimum approach distance; M: specific magnetization.

and **S5**). The trends of the magnetic data (M_S, H_C, etc..) upon Zn substitution resemble those of the 8 nm series, but the SAR for the sample with the smallest amount of zinc reaches 103 W/g, which corresponds to a large heat capability for clinical application. It is worth to stress that the SAR decrease upon further increase of Zn-content (y = 0.26) is confirmed for the 9 nm series (**Figure S10**, SI).

^{1}H-NMR measurements were performed on water dispersions of NPs, stabilized with TMAOH. The nuclear longitudinal relaxivity was evaluated as $r_1 = (1/T_{1,meas} - 1/T_{1,matrix})/C$, where $T_{1,meas}$ is the measured nuclear relaxation time, $T_{1,matrix}$ is the nuclear relaxation time of water and C is the magnetic ion concentration. The NMR-D r_1 profiles, reported in **Figure 8a**, clearly display a scaling behavior as a function of the Zn-content. The evolution of the shape of the curve follows the trend of the magnetic anisotropy previously discussed. The r_1 NMR-D profile of **CoZnFe40** is characterized by a low frequency plateau, a maximum at $v \sim 1.5$ MHz, and a drop of the relaxation rate for higher frequencies. These are typical features of superparamagnetic NPs.[44] On the contrary, the r_1 curve of **CoFe00** displays a plateau at low frequencies and a drop of r_1 for $v > 2$ MHz. This shape is associated to high magnetic anisotropy.[45] Furthermore, an enhancement of the

r_1 values over the whole frequency range is observed when the amount of zinc increases. Using the model by Roch *et al.*[46] to fit the r_1 data, M_S values in good agreement with those obtained by D.C. susceptibility measurements are estimated (**Table 4**).

The nuclear transverse relaxivities r_2 measured at 1.41, 0.36 and 0.17 T (60, 15.5 and 7.2 MHz for ^{1}H, respectively) are shown as a function of the Zn-content in **Figure 8b**. These measurements allowed the investigation of the contrast efficiency of the cobalt zinc ferrite NPs at the typical field used in clinical MRI scanners (e.g., 1.5 T): in particular, the higher the r_2, the higher the contrast efficiency. All the samples proved to be good contrast agents, displaying a transverse relaxivity at least comparable to the commercial superparamagnetic compounds (Endorem is here taken as reference compound). Furthermore, the r_2 value is proportional to the Zn amount, being the highest (r_2~ 515 $s^{-1}mM^{-1}$) for y=0.4.

The influence of the single particle magnetization is crucial for the nuclear spin-spin relaxation of the superparamagnetic NPs since $r_2 \propto M^2$.[46,47] Thus, the r_2 increasing trend found as a function of Zn amount, whereas the M is substantially constant, suggests that some physical mechanisms behind the transverse relaxation are still unclear.[48]

4. Conclusion

A series of Zn-substituted cobalt ferrite NPs with comparable average diameter and variable amount of Zn^{2+} ions was synthesized by thermal decomposition and their structural and magnetic properties were deeply characterized by a wealth of techniques. Since cobalt ions have a strong impact on the magnetic properties of this material, its content was kept constant at approximately x=0.6. This strategy, which to our knowledge has not been explored so far, allowed us to elucidate the effect of Zn substitution on the physical behavior of this complex nanomaterial.

The analysis of the magnetic behavior of the series demonstrated that the expected increase of magnetic moment with progressive Zn substitution, due to the unbalance between *Td* and *Oh* spin sublattices, is preserved only at low temperature. On the contrary, on increasing temperature the thermal disorder decreases the spin alignment degree, and, at room temperature the increase of M_S is retained only for very small amounts of Zn. Moreover, this effect is further counterbalanced by the strong reduction of magnetic anisotropy produced by the insertion of Zn^{2+} ions in the spinel lattice, as indeed demonstrated by magnetic, XMCD and magneto-optical measurements. This behavior can be ascribed to the lattice expansion and local crystal distortion, as well as to the modification in cation distribution following the substitution. These results redefine the expectations relying on Zn-substitution as an effective strategy to improve the performances of cobalt ferrite NPs, particularly in view of their exploitation in biomedical applications. In fact, to assess the impact of these modifications on this landscape, we performed explorative experiments to evaluate the efficiency of the series in the two staple theranostic methodologies, i.e., magnetic fluid hyperthermia and NMR relaxivity. If on one hand the obtained results show that increasing the Zn-content raises the capability of NPs of contrasting MR images, on the other, we found that a value of y between 0.05 and 0.15 increases the hyperthermic efficiency of cobalt ferrite NPs but that any further increase of Zn concentration leads to an opposite effect.

Supporting Information. Supporting information (SI) available: synthesis details; DLS measurement of **CoFe00**; HR-TEM images and electron diffraction patterns; description of the evaluation of the saturation magnetization; *M(H)* curves at room temperature; temperature

dependence of the ZFC-FC magnetizations and temperature kinetic curves of 8 nm NPs; XAS and XMCD spectra of **CoFe00** and orbital and spin contributions to the Co and Fe magnetic moments; TEM images, structural and magnetic properties and SAR values of 9 nm NPs. The following file is available free of charge: M Albino et al_SI_JPCC.pdf

Corresponding Author

*Tel.: +39-0554573270. Fax: +39-0554573372. E-mail: csangregorio@iccom.cnr.it.

*Tel: +39-0554573336. Fax: +39-0554573372. E-mail: claudia.innocenti@unifi.it.

Author Contributions

CI and CS conceived the experiment, EF and MA prepared all the samples and contributed equally. Sample characterization: MA, EF, GB, CI, CJF, CS (structure / magnetism / hyperthermia); CJF, ALO, CS (XMCD); FP, VB, GC, MG (MCD); AL, TO, PA (relaxometry); all the authors participated to data discussion. EF, CI, ALO, FP, PA and CS wrote the manuscript which was critically revised by all the authors.

Acknowledgments

We are grateful to Samuele Ciattini, Francesca Loglio and Laura Chelazzi for helping us with XRD measurements and to Francesco Rugi for ICP analysis. The authors thank the ELETTRA Lightsource for experiments at the Circular Polarization beamline, and Nicola Zema, Stefano Turchini, and Daniele Catone for the support during the measurements. The financial support of COST Action RADIOMAG (TD1402) is gratefully acknowledged.

References

(1) Lee, N.; Yoo, D.; Ling, D.; Cho, M. H.; Hyeon, T.; Cheon, J. Iron Oxide Based

Nanoparticles for Multimodal Imaging and Magnetoresponsive Therapy. *Chem. Rev.* **2015**, *115*, 10637–10689.

(2) Joshi, H. M. Multifunctional Metal Ferrite Nanoparticles for MR Imaging Applications. *J. Nanoparticle Res.* **2013**, *15*, 1235.

(3) Cabrera D.; Coene, A.; Leliaert, J.; Artés-Ibáñez, E. J.; Luc Dupré, L.; Telling, N. D.; Teran, F. J. Dynamical Magnetic Response of Iron Oxide Nanoparticles Inside Live Cells. *ACS Nano* **2018**, *12*, 2741-2752.

(4) Tay, Z. W.; Chandrasekharan, P.; Chiu-Lam, A.; Hensley, D. W.; Dhavalikar, R.; Zhou, X.Y.; Yu, E. Y.; Goodwill, P. W.; Zheng, B.; Carlos Rinaldi, C. et al. Magnetic particle imaging-guided heating in vivo using gradient fields for arbitrary localization of magnetic hyperthermia therapy. *ACS Nano* **2018**, *12*, 3699-3713.

(5) Colombo, M.; Carregal-Romero, S.; Casula, M. F.; Gutiérrez, L.; Morales, M. P.; Böhm, I. B.; Heverhagen, J. T.; Prosperi, D.; Parak, W. J. Biological Applications of Magnetic Nanoparticles. *Chem. Soc. Rev.* **2012**, *41*, 4306–4334.

(6) Ulbrich, K.; Holá, K.; Šubr, V.; Bakandritsos, A.; Tuček, J.; Zbořil, R. Targeted Drug Delivery with Polymers and Magnetic Nanoparticles: Covalent and Noncovalent Approaches, Release Control, and Clinical Studies. *Chem. Rev.* **2016**, *116*, 5338–5431.

(7) Johannsen, M.; Thiesen, B.; Wust, P.; Jordan, A. Magnetic Nanoparticle Hyperthermia for Prostate Cancer. *Int. J. Hyperthermia* **2010**, *26*, 790–795.

(8) Spirou, S. V.; Basini, M.; Lascialfari, A.; Sangregorio, C.; Innocenti, C. Magnetic Hyperthermia and Radiation Therapy: Radiobiological Principles and Current Practice. *Nanomaterials* **2018**, *8*, 401.

(9) Périgo, E. A.; Hemery, G.; Sandre, O.; Ortega, D.; Garaio, E.; Plazaola, F.; Teran, F. J.

Fundamentals and Advances in Magnetic Hyperthermia. *Appl. Phys. Rev.* **2015**, *2*, 0–35.

(10) Fantechi, E.; Campo, G.; Carta, D.; Corrias, A.; de Julián Fernández, C.; Gatteschi, D.; Innocenti, C.; Pineider, F.; Rugi, F.; Sangregorio, C. Exploring the Effect of Co Doping in Fine Maghemite Nanoparticles. *J. Phys. Chem. C* **2012**, *116*, 8261–8270.

(11) Fantechi, E.; Innocenti, C.; Albino, M.; Lottini, E.; Sangregorio, C. Influence of Cobalt Doping on the Hyperthermic Efficiency of Magnetite Nanoparticles. *J. Magn. Magn. Mater.* **2015**, *380*, 365–371.

(12) Sathya, A.; Guardia, P.; Brescia, R.; Silvestri, N.; Pugliese, G.; Nitti, S.; Manna, L.; Pellegrino, T. $Co_xFe_{3-x}O_4$ Nanocubes for Theranostic Applications: Effect of Cobalt Content and Particle Size. *Chem. Mater.* **2016**, *28*, 1769–1780.

(13) Fantechi, E.; Innocenti, C.; Zanardelli, M.; Fittipaldi, M.; Falvo, E.; Carbo, M.; Shullani, V.; Di Cesare Mannelli, L.; Ghelardini, C.; Ferretti, A. M.; et al. A Smart Platform for Hyperthermia Application in Cancer Treatment: Cobalt-Doped Ferrite Nanoparticles Mineralized in Human Ferritin Cages. *ACS Nano* **2014**, *8*, 4705–4719.

(14) Jang, J.; Nah, H.; Lee, J.-H.; Moon, S. H.; Kim, M. G.; Cheon, J. Critical Enhancements of MRI Contrast and Hyperthermic Effects by Dopant-Controlled Magnetic Nanoparticles. *Angew. Chem. Int. Ed. Engl.* **2009**, *48*, 1234–1238.

(15) Bohara, R. A.; Thorat, N. D.; Chaurasia, A. K.; Pawar, S. H. Cancer Cell Extinction through a Magnetic Fluid Hyperthermia Treatment Produced by Superparamagnetic Co–Zn Ferrite Nanoparticles. *RSC Adv.* **2015**, *5*, 47225–47234.

(16) Petitt, G.; Forester, D. Mössbauer Study of Cobalt-Zinc Ferrites. *Phys. Rev. B* **1971**, *4*, 3912–3923.

(17) Lin, Q.; Xu, J.; Yang, F.; Lin, J.; Yang, H.; He, Y. Magnetic and Mössbauer Spectroscopy

Studies of Zinc-Substituted Cobalt Ferrites Prepared by the Sol-Gel Method. *Materials* **2018**, *11*, 1799.

(18) Smit, J.; Wijn, H. P. J.; Philips, N. V. *Ferrites*; Gloeilampenfabrieken: Eindhoven, Holland, 1959.

(19) Mameli, V.; Musinu, A.; Ardu, A.; Ennas, G.; Peddis, D.; Niznansky, D.; Sangregorio, C.; Innocenti, C.; Thanh, N. T. K.; Cannas, C. Studying the Effect of Zn-Substitution on the Magnetic and Hyperthermic Properties of Cobalt Ferrite Nanoparticles. *Nanoscale* **2016, *8*,** 10124-10137.

(20) Carra, P.; Thole, B. T.; Altarelli, M.; Wang, X. X-Ray Circular Dichroism and Local Magnetic Fields. *Phys. Rev. Lett.* **1993**, *70*, 694–697.

(21) Moyer, J. A.; Vaz, C. A. F.; Arena, D. A.; Kumah, D.; Negusse, E.; Henrich, V. E. Magnetic Structure of Fe-Doped $CoFe_2O_4$ Probed by X-Ray Magnetic Spectroscopies. *Phys. Rev. B* **2011**, *84*, 054447.

(22) Huang, D. J.; Chang, C. F.; Jeng, H.-T.; Guo, G. Y.; Lin, H.-J.; Wu, W. B.; Ku, H. C.; Fujimori, A.; Takahashi, Y.; Chen, C. T. Spin and Orbital Magnetic Moments of Fe_3O_4. *Phys. Rev. Lett.* **2004**, *93*, 077204.

(23) Goering, E. J.; Lafkioti, M.; Gold, S.; Schuetz, G. Absorption Spectroscopy and XMCD at the Verwey Transition of Fe_3O_4. *J. Magn. Magn. Mater.* **2007**, *310*, e249–e251.

(24) Jadhav, S. S.; Shirsath, S. E.; Patange, S. M.; Jadhav, K. M. Effect of Zn Substitution on Magnetic Properties of Nanocrystalline Cobalt Ferrite. *J. Appl. Phys.* **2010**, *108*, 093920.

(25) O'Neill, H.S.C.; Navrotsky, A. Simple spinels: crystallographic parameters, cation radii, lattice energies, and cation distribution. *Am. Mineral.* **1983**, *68*, 181.

(26) Hochepied, J. F.; Bonville, P.; Pileni, M. P. Nonstoichiometric Zinc Ferrite Nanocrystals:

Syntheses and Unusual Magnetic Properties. *J. Phys. Chem. B* **2000**, *104*, 905–912.

(27) Coppola, P.; da Silva, F. G.; Gomide, G.; Paula, F. L. O.; Campos, A. F. C.; Perzynski, R.; Kern, C.; Depeyrot, J.; Aquino, R. Hydrothermal synthesis of mixed zinc–cobalt ferrite nanoparticles: structural and magnetic properties. *J. Nanopart. Res.* **2016**, *18*, 138

(28) Raju, K.; Venkataiah, G.; Yoon, D. H. Effect of Zn Substitution on the Structural and Magnetic Properties of Ni–Co Ferrites. *Ceram. Int.* **2014**, *40*, 9337–9344.

(29) Yafet, Y.; Kittel, C. Antiferromagnetic Arrangements in Ferrites. *Phys. Rev.* **1952**, *87*, 290–294.

(30) Coey, J. M. D. *Magnetism and Magnetic Materials*; Cambridge University Press: Cambridge, U.K., 2010.

(31) Cojocaru, S.; Naddeo, A.; Citro, R. Modification of the Bloch Law in Ferromagnetic Nanostructures. *EPL* **2014**, *106*, 17001.

(32) Schieber, M. M. Iron Oxides and Their Compounds. In *Experimental Magnetochemistry*; Wohlfarth, E. P., Ed.; Noth-Holland Publishing Company: Amsterdam, 1967; p 182.

(33) Dormann, J. L.; Fiorani, D.; Tronc, E. Magnetic Relaxation in Fine-Particle Systems. *Adv. Chem. Phys.* **1997**, *XCVIII*, pp. 283–494.

(34) Usov, N. A.; Peschany, S. E. Theoretical Hysteresis Loops for Single-Domain Particles with Cubic Anisotropy. *J. Magn. Magn. Mater.* **1997**, *174*, 247–260.

(35) Hochepied, J. F.; Sainctavit, P.; Pileni, M. . X-Ray Absorption Spectra and X-Ray Magnetic Circular Dichroism Studies at Fe and Co $L_{2,3}$ Edges of Mixed Cobalt–zinc Ferrite Nanoparticles: Cationic Repartition, Magnetic Structure and Hysteresis Cycles. *J. Magn. Magn. Mater.* **2001**, *231*, 315–322.

(36) Skomski, R.; Kashyap, A.; Enders, A. Is the Magnetic Anisotropy Proportional to the

Orbital Moment? *J. Appl. Phys.* **2011**, *109*, 07E143.

(37) Topkaya, R.; Baykal, A.; Demir, A. Yafet–Kittel-Type Magnetic Order in Zn-Substituted Cobalt Ferrite Nanoparticles with Uniaxial Anisotropy. *J. Nanoparticle Res.* **2012**, *15*, 1359.

(38) Tirosh, E.; Shemer, G.; Markovich, G. Optimizing Cobalt Ferrite Nanocrystal Synthesis Using a Magneto-Optical Probe. *Chem. Mater.* **2006**, *18*, 465–470.

(39) Campo, G.; Pineider, F.; Bonanni, V.; Albino, M.; Caneschi, A.; De Julián Fernández, C.; Innocenti, C.; Sangregorio, C. Magneto-Optical Probe for Investigation of Multiphase Fe Oxide Nanosystems. *Chem. Mater.* **2015**, *27*, 466–473.

(40) Mason, W. R. *A Practical Guide to Magnetic Circular Dichroism Spectroscopy*; Wiley-Interscience: New York, 2007.

(41) Kim, K. J.; Lee, H. S.; Lee, M. H.; Lee, S. H. Comparative Magneto-Optical Investigation of d-d Charge-Transfer Transitions in Fe_3O_4, $CoFe_2O_4$, and $NiFe_2O_4$. *J. Appl. Phys.* **2002**, *91*, 9974–9977.

(42) Landi, G. T. Dynamic Symmetry Loss of High-Frequency Hysteresis Loops in Single-Domain Particles with Uniaxial Anisotropy. *J. Magn. Magn. Mater.* **2012**, *324*, 466–470.

(43) Rosensweig, R. E. Heating Magnetic Fluid with Alternating Magnetic Field. *J. Magn. Magn. Mater.* **2002**, *252*, 370–374.

(44) Gossuin, Y.; Gillis, P.; Hocq, A.; Vuong, Q. L.; Roch, A. Magnetic Resonance Relaxation Properties of Superparamagnetic Particles. *Wiley Interdiscip. Rev. Nanomedicine Nanobiotechnology* **2009**, *1*, 299–310.

(45) Orlando, T.; Albino, M.; Orsini, F.; Innocenti, C.; Basini, M.; Arosio, P.; Sangregorio, C.; Corti, M.; Lascialfari, A. On the Magnetic Anisotropy and Nuclear Relaxivity Effects of Co

and Ni Doping in Iron Oxide Nanoparticles. *J. Appl. Phys.* **2016**, *119*, 134301.

(46) Roch, A.; Muller, R. N.; Gillis, P. Theory of Proton Relaxation Induced by Superparamagnetic Particles. *J. Chem. Phys.* **1999**, *110*, 5403–5411.

(47) Vuong, Q. L.; Berret, J.-F.; Fresnais, J.; Gossuin, Y.; Sandre, O. A Universal Scaling Law to Predict the Efficiency of Magnetic Nanoparticles as MRI T_2-Contrast Agents. *Adv. Healthc. Mater.* **2012**, *1*, 502–512.

(48) Gossuin, Y.; Orlando, T.; Basini, M.; Henrard, D.; Lascialfari, A.; Mattea, C.; Stapf, S.; Vuong, Q. L. NMR Relaxation Induced by Iron Oxide Particles: Testing Theoretical Models. *Nanotechnology* **2016**, *27*, 155706.

TOC Graphic